Chapter-4

Anhydrous CoC_2O_4 nanorods for pseudocapacitive energy storage applications

4. 1 Introduction

Most oxide materials suffer from structural instability and performance degradation issues [1-3]. Metal-organic frameworks (MOFs) are open framework structures where materials are constructed by joining metal-containing units with organic linkers creating permanent porosity [4]. Porous metal oxalate materials were studied to have faradaic pseudocapacitive characteristics, a reversible redox reaction mechanism seems to operate on the surface of metal oxalates[5].

In this chapter, we present the synthesis of anhydrous CoC_2O_4 Nanorods in a two-step process and electrochemical study of the electrode in the aqueous electrolyte that shows the superior performance of the electrode for pseudocapacitor applications. Superior specific capacitive charge storage close to 2116 F g^{-1} at 1 A g^{-1} was observed for porous anhydrous CoC_2O_4 Nanorods compared to capacitance equivalent to 840 F g^{-1} at 1 A g^{-1} for hydrated $CoC_2O_4.2H_2O$ in aqueous 2M KOH electrolyte. Further, electrode performances were studied in Asymmetric supercapacitors (ASCs) mode in which porous anhydrous CoC_2O_4 nanorods were made as the positive electrode and Activated Carbon (AC) as the negative electrode and a highest specific energy equivalent to 129 W h kg^{-1} and specific power 647 W kg^{-1} was obtained at 0.5 A $g^{-1.}$ Synthesis, characterizations of porous anhydrous CoC_2O_4 nanorod, and the detailed electrochemistry developed electrodes are presented in this chapter.

4.2 Material synthesis and characterization

4.2.1 Synthesis

Synthesis of porous anhydrous CoC_2O_4 nanorod was carried out by a two-step process. 2.91 g (10 mM) of $Co(NO_3)_2.6H_2O$ was dissolved in 200 ml of deionized water with continuous stirring in a beaker placed at a hot plate magnetic stirrer and 1.27 g (10 mM) $H_2C_2O_4.2H_2O$) were added in the solution. The entire mixture was stirred vigorously at 80ºC for 3 h. After

3h of stirring green color powder, $CoC_2O_4.2H_2O$ was precipitated. The obtained product is then washed several times with deionized water. Finally, the washed product $CoC_2O_4.2H_2O$ was dried in a hot air oven at 90 ºC overnight. Anhydrous CoC_2O_4 was produced after heating the materials at 220 ºC for 3 h. The formation of Anhydrous CoC_2O_4 can be represented by the following equations given below;

$$Co(NO_3)_2.6H2O + H_2C_2O_4.2H_2O \longrightarrow CoC_2O_4.2H_2O \downarrow + 2HNO_3 + 2H_2O \quad \text{at } 80^oC \quad (4.1)$$

$$CoC_2O_4.2H_2O \longrightarrow CoC_2O_4 + 2H_2O \uparrow \quad \text{above } 200^oC \quad (4.2)$$

4.2.2 Characterizations

The crystal structure and phase purity of synthesized products were characterized through RigakuMiniflex desktop X-ray diffractometer (XRD) with Cu-Ka radiation (l ¼ 0.154 nm) in the 2θ range of 10–90º with a step size of 0.02º. Xpert High Score (PANanylytical) software was used to identify the required phase. FE-SEM (FP 5022/22) was used to determine the surface morphology and particle size distribution of the samples. Infrared spectra of the samples were recorded using Nicolet iS5 FTIR spectrometer in the range of 400 to 4000 cm^{-1}. Pore size distribution and specific surface area of the sample were measured by BET (MicrotracBEL). All electrochemical performances of the sample including cyclic voltammetry (CV), galvanostatic charge-discharge (GCD), and electrochemical impedance spectroscopy (EIS) measurements were conducted in a conventional three-electrode arrangement and measured by Metrohm Autolab (PGSTAT204) equipped with FRA32 M module. Electrochemical measurements were analyzed using NOVA1.1 software.

4.2.3 Preparation of Electrode

Hydrated $CoC_2O_4.2H_2O$ and anhydrous porous CoC_2O_4 working electrodes were prepared by taking active material, activated carbon (AC), and binder polyvinylidene difluoride (PVDF) in the ratio of 7: 2: 1 in N-methyl-2-pyrrolidone (NMP) solvent. The homogenous slurry was

prepared in the mortar and the slurry was cast over Toray carbon paper. The materials (paste) loading was 1 mg over 1 cm^2 area of. The coated electrode was dried at 80 ºC for 12 h.

4.3 XRD Study

The powder XRD pattern of prepared $CoC_2O_4.2H_2O$ and anhydrous CoC_2O_4 sample in the 2θ range of 10–60º with step size 0.02º. Phase identification was done by Philips x'pert highscore. The prominent sharp diffraction peak of $CoC_2O_4.2H_2O$ matches well with the β-orthorhombic phase (space group: Cccm, JCPDS no. 25-0250) with lattice parameter a =11.877Å, b = 5.419Å, and c =15.624Å [6]. As confirmed by the XRD study, After annealing at 220 ºC for 5 h, $CoC_2O_4.2H_2O$ was transformed to anhydrous CoC_2O_4 in a-monoclinic structure (space group P21/n, JCPDS no. 37-0719), Figure 4.1(b) shows Rietveld Refinement powder XRD pattern of CoC_2O_4 and inset show the VESTA image of the crystal. The lattice parameter of anhydrous CoC2O4 was found to be a = 5.26400Å, b= 5.66000Å, c =7.17900Å with cell angle equivalent to α – 90º, β – 118.88º,γ – 90º [7].

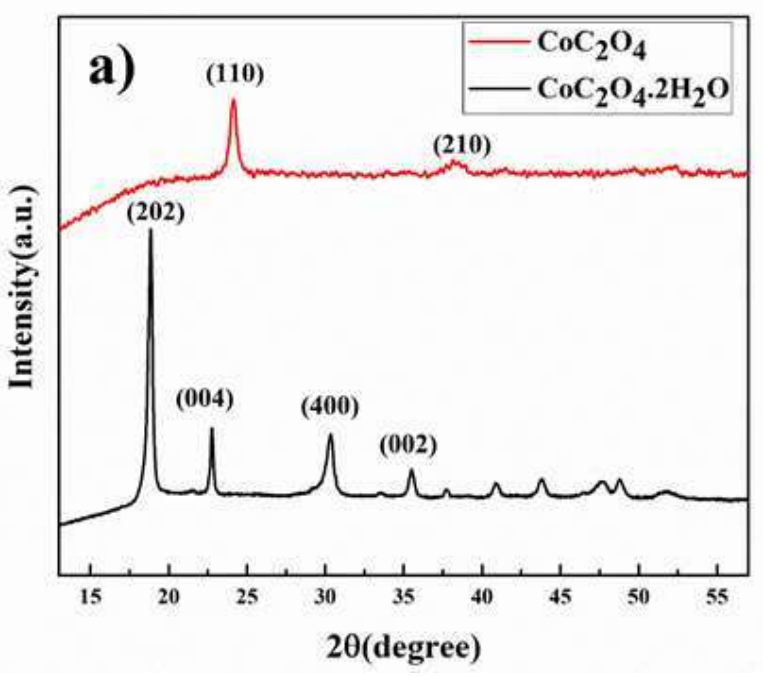

Figure. 4.1 (a) XRD pattern of $CoC_2O_4.2H_2O$ and CoC_2O_4

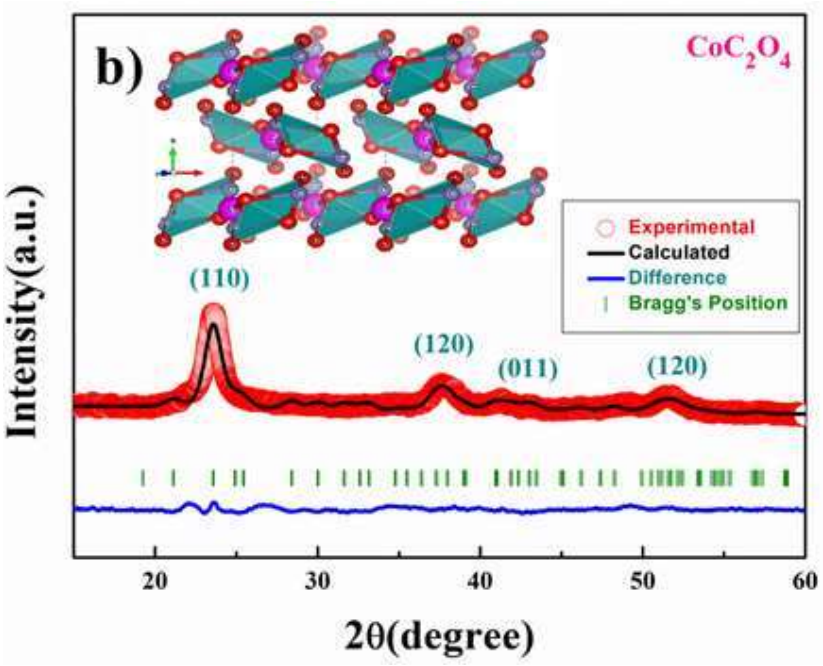

Figure. 4.1 (b) Rietveld refinement powder XRD pattern of CoC_2O_4 (vista image in inset),

4.4 Thermal study

The thermos-gravimetric analysis (TGA) curve shown in Figure 4.1(c) was carried out to quantitatively analyze the weight loss-assisted phase transformation. First weight loss occurred from 100–300 ºC, which corresponds to the removal of structural water from the sample between this temperature range resulting in phase formation of anhydrous CoC_2O_4 in monoclinic structure. TGA curve determines the weight loss equivalent to 19.66% or 2mole of water per molecule between this temperature. Similarly, the second weight loss step equivalent to 37.25% occurs in the temperature range of 350–500 ºC due to the decomposition of CoC_2O_4 [8]. The weight losses can be represented as:

$CoC2O4.2H2O \rightarrow CoC2O4 + 2H2O$ (aboveT~200 ºC) (4.3)

$CoC2O4 \rightarrow Co + 2CO2$ (above T~ 450 ºC) (4.4)

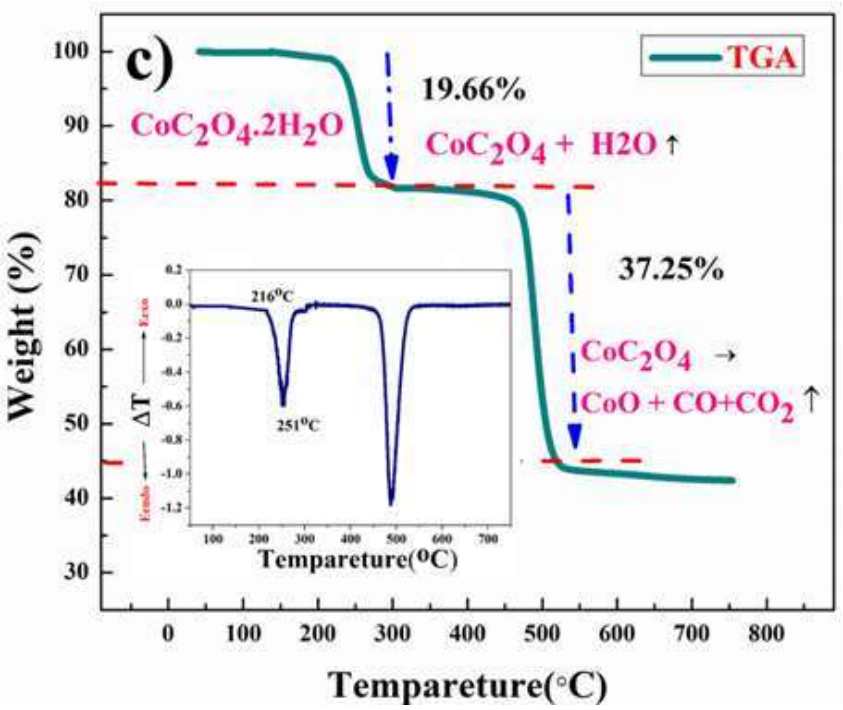

Figure. 4.1 (c) Thermogravimetric analysis (TGA) of $CoC_2O_4.2H_2O$

The Differential Thermal Analysis (DTA) curve presents in the inset of Figure 4.1(c). The rate of weight loss reaches to peak at 250 ºC with the peak starting at 216 ºC. That is why we did calcinations or water removal step at 220 ºC to get controlled or slow water release to preserve the high surface area of the material to stop or avoid particle segregation.

FTIR spectrums of $CoC_2O_4.2H2O$ and anhydrous CoC_2O_4 powder samples are shown in Figure 4.1(d) revealing the presence of different functional groups at different wavenumber (cm^{-1}). The broad peak at 3385.84 cm^{-1} is ascribed to the stretching vibration of a hydroxyl group (–OH) which signifies the presence of water in the compound. The observed peak at 1620.75 cm^{-1} was assigned for the anti-symmetric carbonyl stretching band (C=O) specific to the oxalate group [12]. Two weak peaks at 1365.52 cm^{-1} and 1323.1 cm^{-1} were attributed to vibrations of $C_2O_4^{2-}$ (C–O) + (C–C) and (C–O) + (O–C=O), respectively. The peak at 819.16 cm^{-1} was assigned to the vibration mode of $C_2O_4^{2-}$, O–C=O bending vibrations (O–C=O).

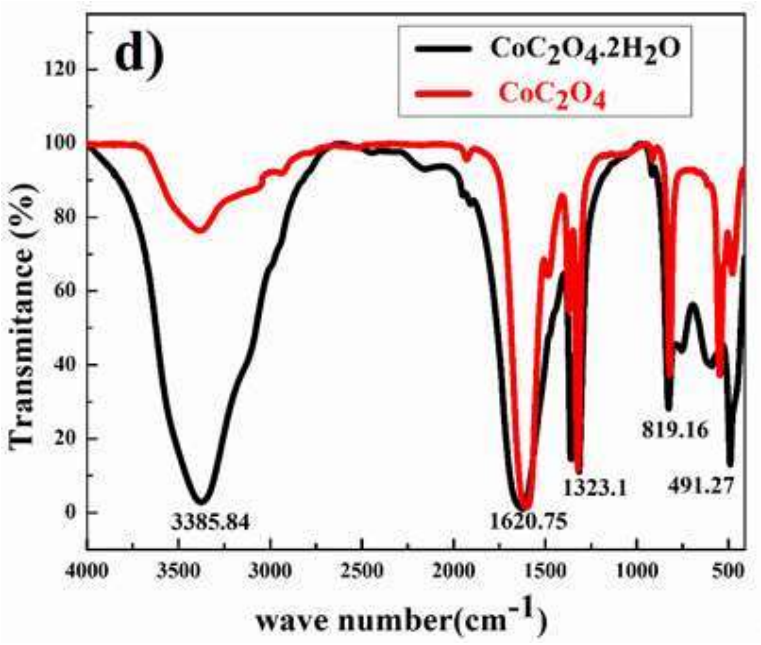

Figure. 4.1: (d) FT-IR spectra of $CoC_2O_4.2H_2O$ and CoC_2O_4

The absorption peak at 491.27 cm^{-1} can be attributed to Co–O bonding present in a prepared sample of $CoC_2O_4.2H_2O$. Compared to $CoC_2O_4.2H_2O$, almost negligible peak strength for stretching vibration of the hydroxyl group (–OH) near 3385.84 cm^{-1} was observed in an anhydrous CoC_2O_4 sample prepared by heating at 220 ºC for 3 h as shown in Figure 4.1(c).[9] Rest vibration frequencies are observed almost at the same position as $CoC_2O_4.2H_2O$.

The BET surface area measurement results for $CoC_2O_4.2H_2O$ and anhydrous CoC_2O_4 samples are shown in Figure 4.1(e). Large nitrogen absorption/desorption isotherm was observed for anhydrous CoC_2O_4 compared to $CoC_2O_4.2H_2O$. The nitrogen adsorption and desorption isotherm show characteristics which are corresponding to the mesoporous structure for the anhydrous cobalt oxalate (CoC_2O_4) sample. The calculated BET-specific surface area and average pore diameter were found 60.9 m^2g^{-1} and 3.72 nm, respectively. Mesopore structures can contribute to excellent electrochemical performance due to high porosity. The calculated mesopores diameter of the CoC_2O_4 sample is much bigger than the ions present in aqueous electrolytes.[10-11]

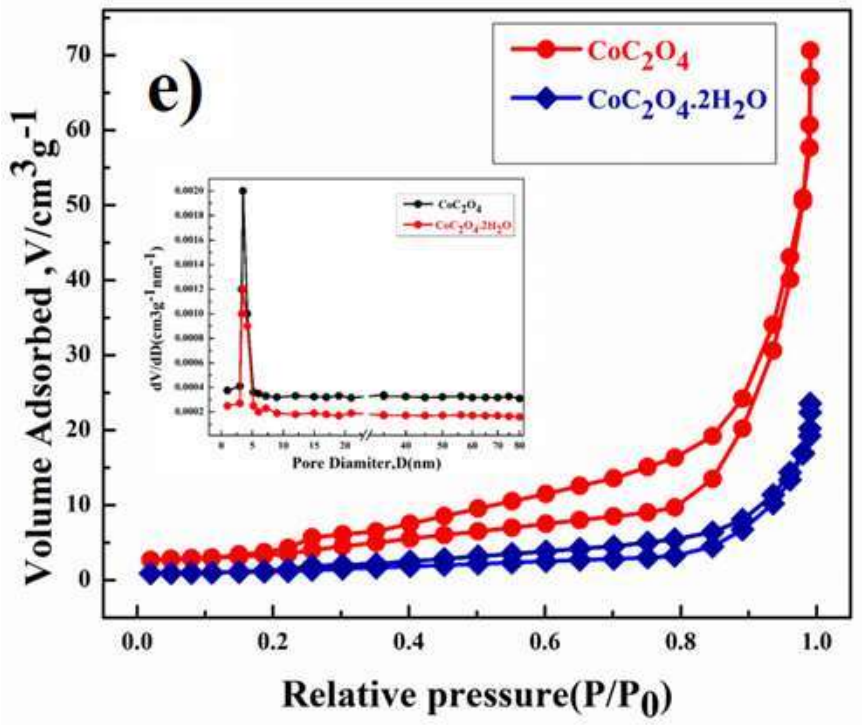

Figure. 4.1: (e) BET surface area measurement plot of $CoC_2O_4.2H_2O$ and CoC_2O_4.

The X-ray photoelectron spectroscopy (XPS) survey of the anhydrous CoC_2O_4 sample confirming the presence of Co shows in Figure 4.2(a). The Co (2p) spectrum shown in Figure 4.2(b) are assigned to $2p_{3/2}$ at 778.84 eV and $2p_{1/2}$ at 797.87 eV along with corresponding satellite peaks at 782.3 eV and 798.87 eV for Co^{2+} ions [12]. Figure 4.2(c) shows the O 1s spectra consisting of the merger of two peaks for corresponding binding energy at 527.98 eV for C–O bonding and at 528.78 eV for C=O bonding.

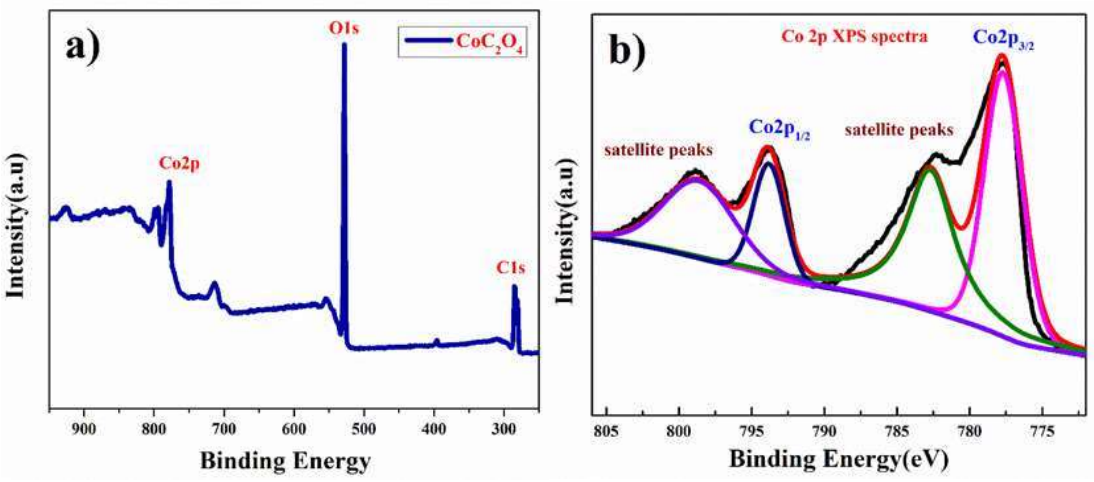

Figure. 4.2: XPS plot of (a) full survey CoC_2O_4 nanorods (b) Co (2p)

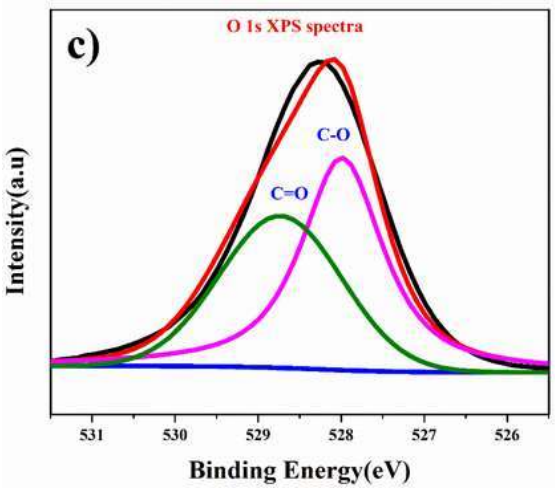

Figure. 4.2: (c) XPS plot of CoC_2O_4 nanorods O (1s).

4.5 SEM/EDAX Study

SEM image is shown in Figure 4.3(a) particle size distribution and flakes type morphology of $CoC_2O_4.2H_2O$ power sample. Figure 4.3(b) shows particle size distribution and morphology of the anhydrous CoC_2O_4 power sample. Nanorods type particle morphology was visible in the range of 300–700 nanometre size with an average particle size approaching 487 nm as analyzed by ImageJ software. The slow release of a water molecule in the control dehydration step (calcinations at 220 ºC) resulted in the formation of nanorods of anhydrous CoC_2O_4. Figure 4.3(b) shows the (energy dispersive X-ray analysis) result and elemental

analysis confirm the composition of anhydrous CoC_2O_4. TEM image shown in Figure 4.3(d) represent single particle and atomistic arrangements at localized regions of the powder materials grown as a single rod with a diameter of 160 nm and length of 960 nm. The insert images represent FFT (Fast Furrier Transformation) and inverse FFT of the sample particle. Figure 4.3(e) represents of calculated d spacing 0.358 nm of the (110) plane for the anhydrous CoC_2O_4 phase.

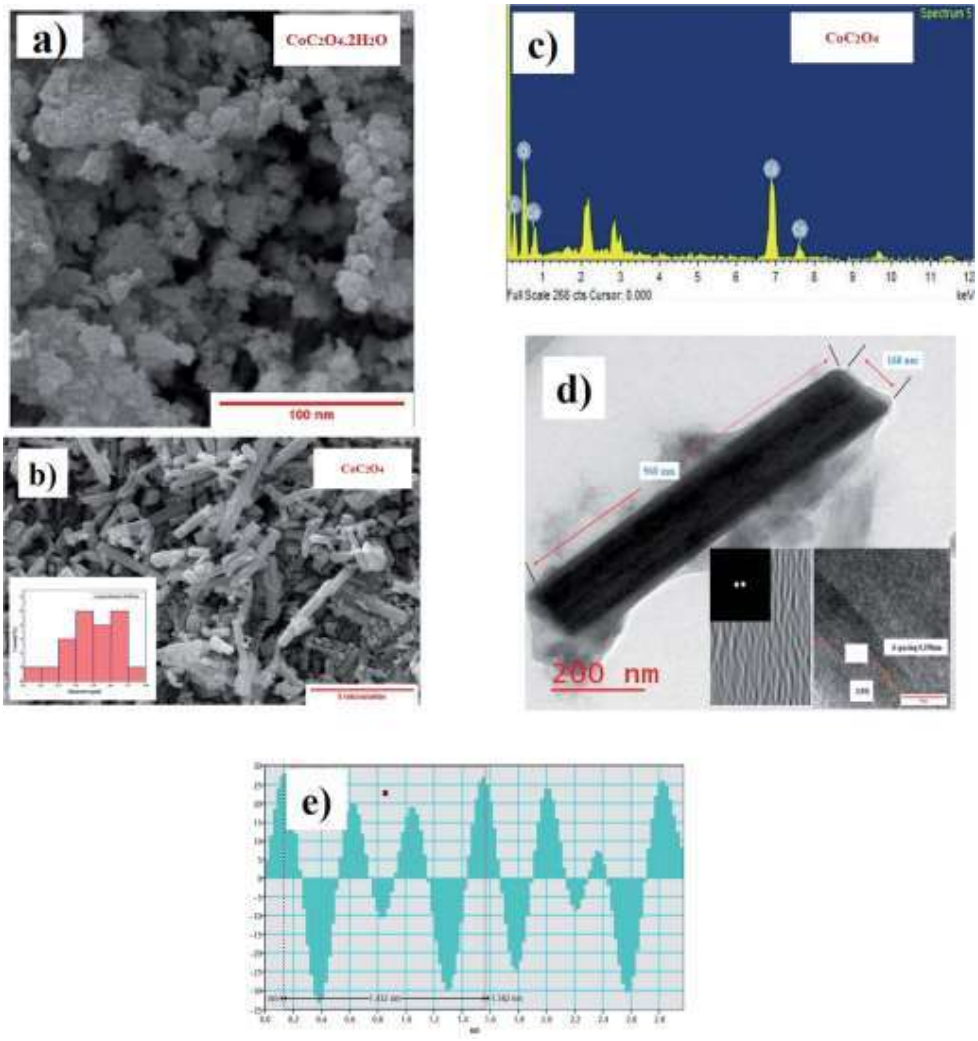

Figure 4.3 (a) SEM image showing flakes type morphology and particle size distribution of $CoC_2O_4.2H_2O$, (b) SEM image showing morphology and particle size distribution of anhydrous CoC2O4 nanorods, (c) EDX of anhydrous CoC_2O4 nanorods, (d) TEM image at localized regions showing single rod (with FFT and inverse FFT) and (e) (110) plane d spacing of anhydrous CoC_2O4

4.6 Electrochemical Studies

Electrochemical studies Electrochemical performance of $CoC_2O_4.2H_2O$ and porous anhydrous CoC_2O_4 as a working electrode were characterized using a three-electrode system where $CoC_2O_4.2H_2O$ and porous anhydrous CoC_2O_4 act as a working electrode, Hg/HgO (1 M KOH) as a reference electrode, and Platinum as counter electrode in 2 M KOH as an electrolyte. The charge storing capacity of $CoC_2O_4.2H_2O$ and porous anhydrous CoC_2O_4 electrodes were mainly calculated using cyclic voltammetry (CV) curve between the potential range of 0 V to 0.30 V. Figure 4.4(a) represents the CV curve of $CoC_2O_4.2H_2O$. The nature of the curve represents pseudo capacitive charge storage behavior coupled with surface redox (electrosorption). Figure 4.4(b) presents the CV curve of porous anhydrous CoC_2O_4 nanorods representing pseudo-capacitive storage couple with surface redox and anion intercalations.[13a] Redox peaks originated due to the reversible transformation between Co^{2+} to Co^{3+} during electrosorption (redox) of OH ion. $Co^{2+/3+}$ redox peak appears around 0.17 V vs. Hg/HgO reference electrode. The nanostructuring seems to play important role in lowering the redox peak ($Co^{2+/3+)}$ on anhydrous CoC2O4 nanorods compared to the redox peak reported in the literature [13b].

$$Co(II)C_2O_4.2H_2O + OH^-_{sol} \longleftrightarrow Co(III)(OH^-)C_2O_4.2H_2O + e^- \quad (4.5)$$

$$Co(II)C_2O_4 + OH^-_{sol} \longleftrightarrow Co(III)(OH^-)C_2O_4 + e^- \quad (4.6)$$

From the CV curve, the specific capacitance C (F/g) can also be calculated as one of the significant parameters to understand the electrochemical performance of the working electrode. [14]

$$Csp = \frac{\int i\,(V)\,dV}{2mV\vartheta} \quad (4.7)$$

where 'm' is the mass of active material in the electrode (g), 'V' is the potential window (V) and 'ϑ' is the scan rate (mV/s). The specific capacitances of $CoC_2O_4.2H_2O$ and Highly Porous non-hydrate CoC_2O_4 were calculated using equation (4.7) and capacitance was found

close to 604F/g, 1636F/g at 1mV/s. Comparative CV curves for $CoC_2O_4.2H_2O$ and anhydrous CoC_2O_4 nanorods at a scan rate of 10 mVs^{-1} are shown in Figure 4.4(c) and this demonstrated that two different types of phenomena occur during the charge storage process; at $CoC_2O_4.2H_2O$ electrode, it is diffusion control surface redox and at pores CoC_2O_4 nanorod electrodes it is diffusion control surface redox (faradaic process) coupled with intercalation of ions (OH).[13] As superior capacitance was obtained for anhydrous porous CoC_2O4 nanorods, hereafter we mainly present the study significantly on this sample only.

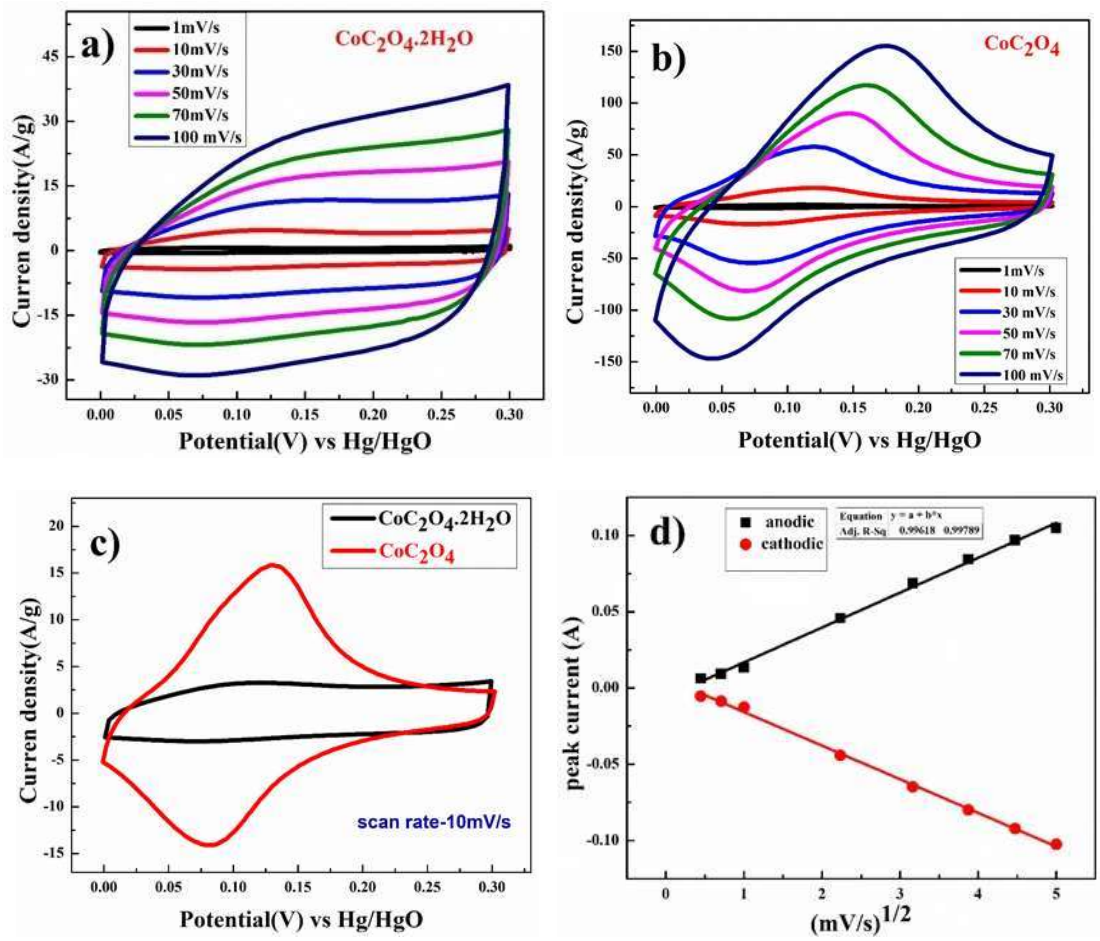

Figure. 4.4: (a) Cyclic voltammetry of $CoC_2O_4.2H_2O$ (b) cyclic voltammetry of anhydrous CoC_2O_4 nanorods (c) comparative cyclic voltammetry of $CoC_2O_4.2H_2O$ and CoC_2O_4 nanorods at 10 mV s1 and (d) plot of log (peak current) vs. square root of scan rate.

Figure 4.4(d) shows the linear relation between anodic and cathodic peak current with respect to the square root of scan rate, indicating that CoC_2O_4 exhibits a semi-infinite diffusion controlled process. Furthermore, the electrode kinetics of electrode can be understood by determining the diffusion coefficient. The diffusion coefficient for the electrode was determined using Randles-Sevick equation (4.8) [15]

$$i_p = 2.686 \times 10^5 \times n^{3/2} A D^{1/2} C_o v^{1/2} \quad (4.8)$$

Where i_p is peak current (A), n is the number of electrons transferred in the redox event (usually 1), A is electrode area in cm^2, D is diffusion coefficient in cm^2/s, C_o is OH^- ion concentration in mol/cm^3, ν is scan rate in V/s. According to eq. OH^- the diffusion coefficient of CoC_2O_4 was found to be 7.65×10^{-9} cm^2/s for oxidation and 6.11×10^{-9} cm^2/s for the reduction cycle.

To further understand the diffusion mechanism qualitatively to differentiate the charge storage kinetics of different ranges of charge storage from battery type to supercapacitors mode, the power law equation given below was used.

$$i = av^b \quad (4.9)$$

where a and b are adjustable values, i is the current (A), and ν is the scan rate (V/s). The value of b lies between 0.5 to 1, b= 0.5 stands for the semi-infinite diffusion control reaction i.e. battery type material while b = 1 stands for the capacitive control reaction.[16] Figure 4.5(a) shows the slopes of the corresponding log(peak current(i_p) vs log (v) plots, when scan rates ranging from 1 to 10 mV s^{-1}, the b-value for both cathodic and anodic peaks was found to be 0.65 and 0.63, demonstrating that the rate kinetics are controlled by diffusion control surface redox dominating, and thus are very fast. This limitation to the rate capability at higher current rates can arise from numerous sources including an increase of the ohmic contribution (active material resistance, solid/electrolyte interphase resistance) and/ or diffusion constraints/limitations [17].

As shown in Figure 4.5(b), voltammetry sweep rate dependence can distinguish quantitatively the capacitive contribution to the current response. The current response at a fixed potential is the combination of two separate mechanisms, surface capacitive effects, and diffusion-controlled insertion.

$$i(\upsilon) = k_1 v + k_2 v^{\frac{1}{2}} \qquad (4.10)$$

For more understanding equation (4.10) was modified

$$\frac{i(\upsilon)}{\upsilon^{\frac{1}{2}}} = \frac{k_1}{\upsilon^{\frac{1}{2}}} + k_2 \qquad (4.11)$$

From equation (4.10) $k_1 \upsilon$ and $k_2 \upsilon^{1/2}$ define the current contributions from the surface capacitive effects and the diffusion-controlled intercalation process, respectively. Thus after the determination of k_1 and k_2, it can be able to quantify, at specific potentials, the fraction of the current due to each of these contributions can be quantified.[18] The Values for k_1 and k_2 are determined from the slope and intercept of the y-axis from the linear fitting of the curve. The representative curve of $i(V)/v^{1/2}$ *vs.* $v^{1/2}$ is shown in Figure 4.5(b). The contribution of surface capacitance and diffusion-controlled interaction at different scan rates are shown in Figure 4.5(c). After the determination of k_1 and k_2 values, Figure 4.5(d) represents the contribution of surface capacitance (69%) and diffusion-controlled interaction (31%) at peak potential (0.155 V) at a scan rate of 10 mV s^{-1}. According to Trassati, the total specific capacitance is the sum of the inner and outer surface capacitance of the electrode and it can be expressed as.

$$C_{total} = C_{in} + C_{out} \text{ (F /g)} \qquad (4.12)$$

The specific capacitance contributions from the inner and outer surface of the electrode also depend upon the scan rate.[19] As shown in Figure 4.5(e), the y-intercept of the linear fit (1/q vs. $v^{1/2}$ plot at $v = 0$) shows the amount of total charge stored at the electrode. As shown in Figure 4.5(f), the y-intercept of the linear q vs. $v^{-1/2}$ plot at $v = \infty$ represents corresponds to the amount of charge stored at the outer surface of the electrode. After applying Trassati plot

outcomes, it can be concluded that the total capacitance value C_{total} was found to be 1636 F g^{-1}, C_{in} was found to be 1233 F g^{-1} (75% of total capacitance value) and C_{out} was found to be 403 F g^{-1}(25% of total capacitance value).

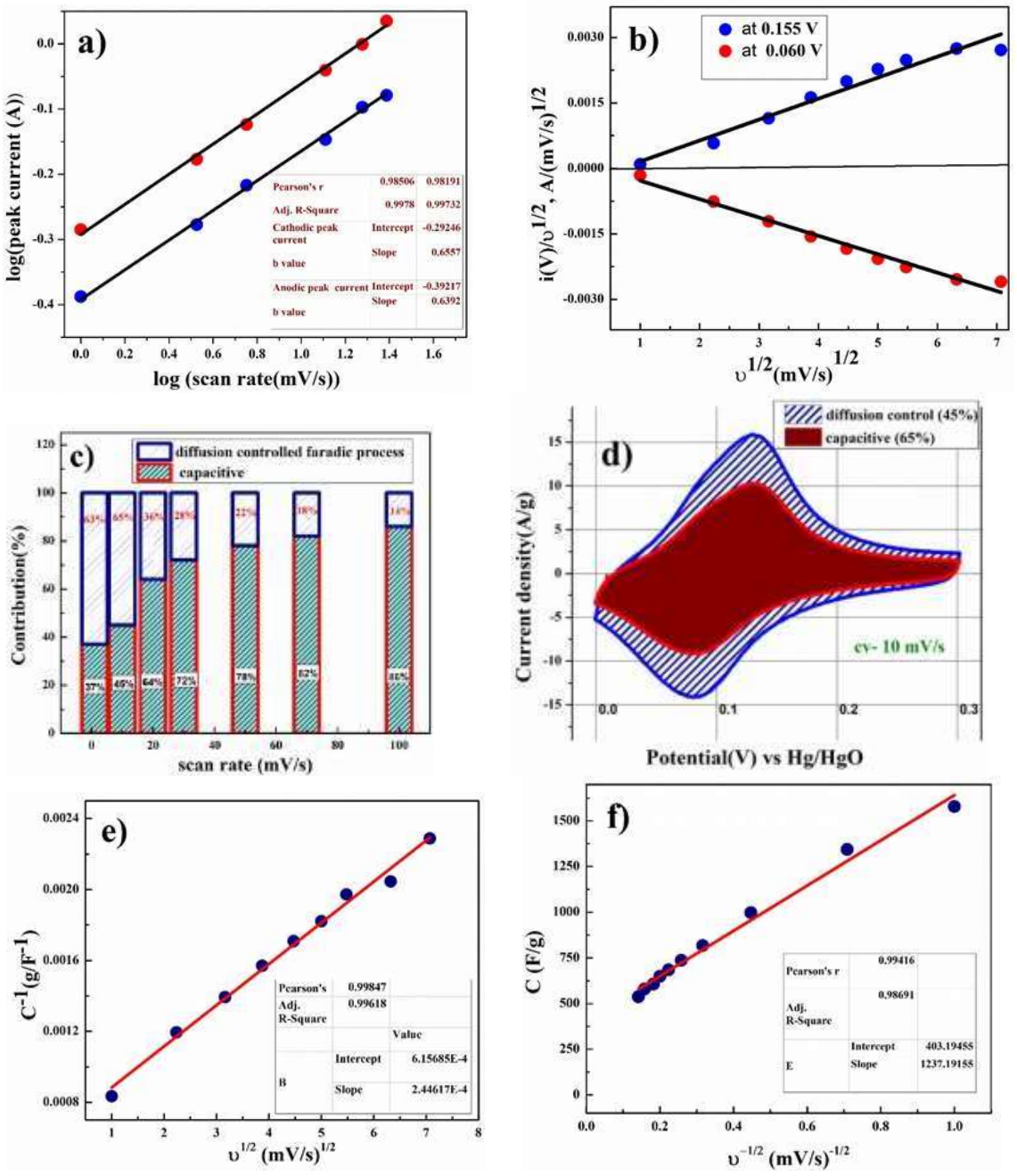

Figure 4.5: (a) Plot of the linear relationship between log (peak current) and log(scan rate) at two different scan rate regions, (b) plot of power's law of charged state at a potential and discharged state at a potential, (c) contribution of diffusive and capacitive at different scan rates contribution, (d)analysis of kinetic contribution at 10 mV s^{-1} and (e and f) corresponds to Trasatti plot.

Galvanostatic charge-discharge experiments were performed for more accurate capacitance measurements of $CoC_2O_4.2H_2O$ and porous CoC_2O_4 nanorod electrodes. From the charge-discharge curve, the specific capacitance of the electrode can be calculated as:[14]

$$Csp = \frac{I\Delta t}{m\Delta V} \quad (4.13)$$

where I is the discharge current (A), Δt the discharge time (s), m is the mass of the active material in the electrode (g) and ΔV is the potential change during discharge (V). Figure 4.6(a) depicts the specific capacitances of $CoC_2O_4.2H_2O$ electrodes equivalent to 840 F g^{-1}, 576 Fg^{-1}, and 292 F g^{-1}, at current densities of 1, 2, and 3 A g^{-1}. Figure 4.6(b) represents the specific capacitances of porous anhydrous CoC_2O4 nanorods electrodes equivalent to 2116 F g-^{1}, 1403 F g^{-1}, 390 F g^{-1}, 186 F g^{-1}, at current densities of 1, 2, 5 and 10 A g^{-1} current rates. It has been observed that with the increase in current density there was a decrease in the specific capacitance of the materials. Figure 4.6(c) shows the capacitance vs. no. of cycles plot at different constant current rates for porous CoC_2O_4 nanorod electrodes. Figure 4.6(d) exhibits excellent long-term cycle stability and capacity retention of porous CoC_2O_4 nanorod electrodes at the current rate of 3 A g^{-1} for 2200 cycles. Around 95% capacity retention was observed for the electrodes indicating that specific capacitance wasn't changed much from the initial capacitance value even after the 2200 cycle. Simultaneously, coulombic efficiency ($\eta=t_d/t_c$) of the electrode was found ~97% after 2200 cycles of charge/discharge that reveals the superior stability of the porous CoC_2O_4 nanorod electrodes. In addition to the electrochemical stability test, we also performed AC EIS measurements as shown in the Nyquist plot at OCP in Figure 4.6(e) in the frequency range (1 MHz to 0.1 Hz). The specific impedance contribution is mainly attributed to the impedance distributions over electric series resistance (R_s), charge transfer resistance (R_{ct}), and Warburg impedance (R_w). At higher frequency, for $CoC_2O_4.2H_2O$ and porous CoC_2O_4 nanorod electrodes, the intercept in the EIS spectra on the real axis was found at 1Ω and 0.5Ω respectively indicating very small internal

resistance. The small semicircle in the high-frequency region also shows the fast charge transport between electrode and electrolyte. Lower frequency data represent the Warburg diffusion resistance and for porous CoC_2O_4 electrode samples, the straight line in the low-frequency region is close to 90° angle (very close to -Z''(Ω) axis) from the horizontal line represents the characteristic of pseudo capacitance behavior. This also represents fast OH^- ion diffusion in the porous structure.[20]

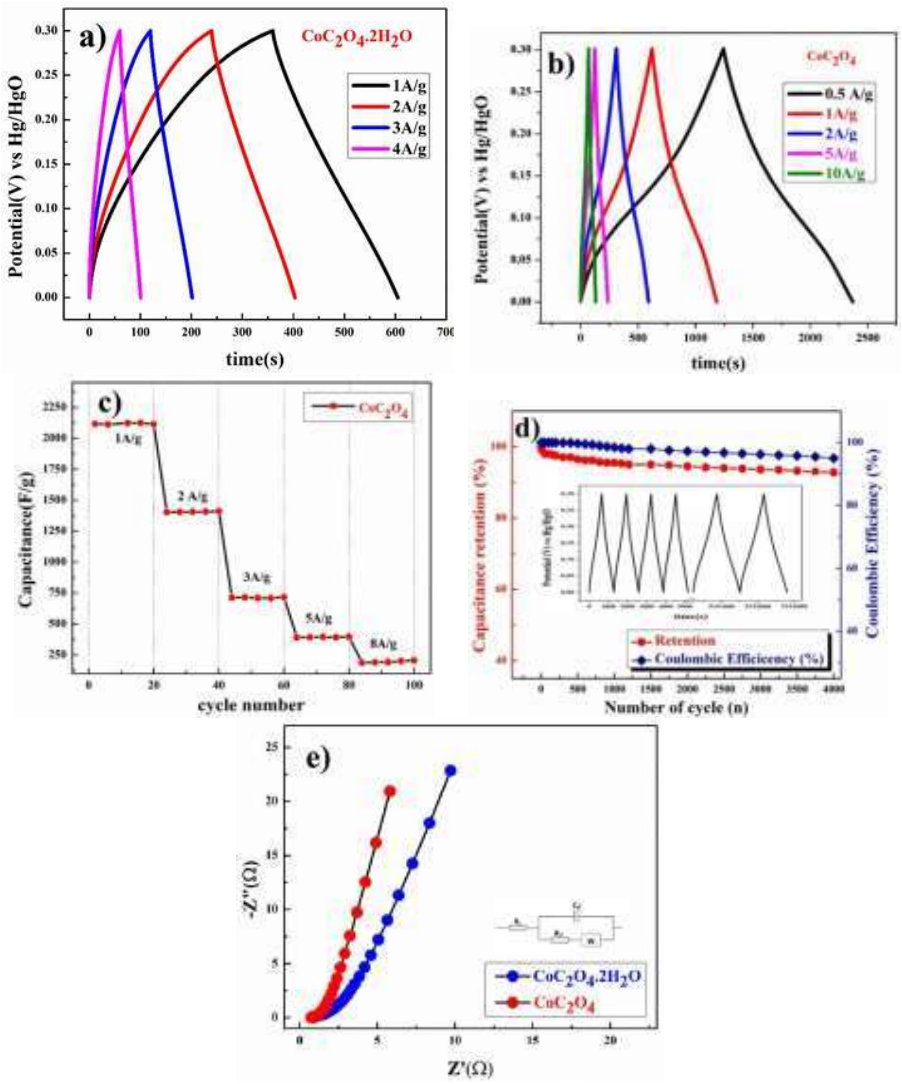

Figure. 4.6: (a) Charge–discharge curve of $CoC_2O_4.2H_2O$, (b) charge–discharge curve of CoC_2O_4 nanorods, (c) capacitance performance of CoC_2O4 nanorods at different constant current rates, (d) capacitance retention and coulombic efficiency of porous CoC_2O_4 nanorods and (e) EIS plot of $CoC_2O4.2H_2O$ and porous CoC_2O_4 nanorods at 10 mV.

Further studies were conducted to understand the effects of anions present in the electrolyte. Figure 4.7(a) shows the completely non-rectangular shape CV curve for porous CoC_2O_4 nanorods as an electrode in KOH and Na_2SO_4 electrolytes. The redox peak was dominant in KOH compared to Na_2SO_4, which was due to the size difference of hydration radii of sulfate ions (3.79 Å) compared to hydroxyl ions (3 Å). A larger hydration sphere of SO_4^{2-} causes a decrement of ions entering into the pores, causing thinner electric double layer formation. In addition, KOH exhibits a higher current response in the CV curve also due to its higher molar conductivity OH^- ion (198 $cm^2\ \Omega\ mol^{-1}$) compared to SO_4^{2-} (79.8 $cm^2\ \Omega\ mol^{-1}$) in Na_2SO_4.[21] As specific capacitance function of scan rate has been estimated using equation (4.7), wherein 2 M KOH exhibits a higher specific capacitance of 1236 F g^{-1} observed compared to 366 F g^{-1} specific capacitance at 10 mV s^{-1} in 0.5 M Na_2SO_4 electrolyte. GCD experiments were performed for determining the quantitative aspect of capacitance assessment in KOH and Na_2SO_4 using Eqn (4.13). Figure 4.7(b) GCD curve in the different electrolytes, in 2MKOH electrolyte. Specific capacitance was found to be 2116 F g^{-1} and in 0.5 M Na_2SO_4 electrolyte, it was found to be 973 F g^{-1} at 1 A g^{-1}. This study confirms the suitability of aqueous KOH electrolyte for the high performance of the electrode as a smaller size of OH^- ion results easily diffusion to result in superior performances.

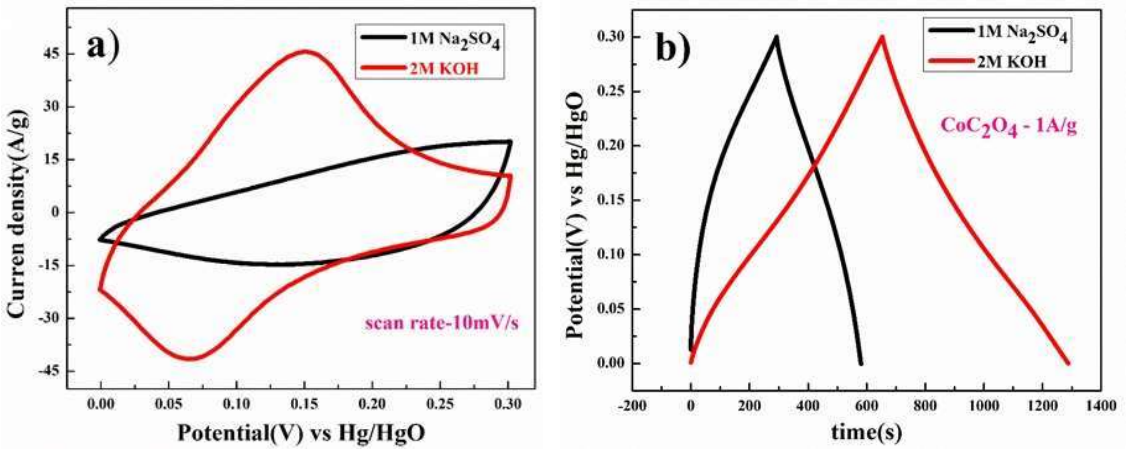

Figure.4.7: (a) CV and (b) charge-discharge of porous anhydrous CoC_2O_4 nanorods at 10 mV s^{-1} in 2 M KOH and 0.5 M Na_2SO_4.

4.7 Two electrode tests

To understand the real charge storage behavior of porous anhydrous CoC_2O_4, two electrode measurements have been conducted in a 2 M KOH electrolyte using AC (activated carbon) as the counter electrode. To determine the maximum specific capacitance during the full test, the storage capacity of positive and negative electrodes need to be balanced as per the following equation:

$$\frac{1}{C_{total}} = \frac{1}{C_{positive}} + \frac{1}{C_{negative}} \qquad (4.14)$$

For balancing the charge storage capacity of the cell, the mass ratio (m^+/m^-) of positive and negative electrode materials was measured using the following equation:

$$\frac{m^+}{m^-} = \frac{C_- \times \Delta E_-}{C_+ \times \Delta E_+} \qquad (4.15)$$

m^+, m^-, C_+, C_-, ΔE_+, ΔE_- are mass, specific capacitance, and potential window of positive and negative electrodes estimated by three-electrode measurement.[22-23]

Figure 4.8(a) shows the CV curve at a 10 mV s^{-1} scan rate using AC (activated carbon) as the negative electrode and porous anhydrous CoC_2O_4 positive electrode. Calculated mass ratio $\frac{m^+}{m^-}$ was kept 1:3.54 for the asymmetric cell, weight of the active material was 4.54 mg (excluding the weight of Activated Carbon and PVDF). Figure 4.8(b) demonstrates the CV curve of porous CoC_2O_4//AC in two electrodes ASCs (Asymmetry Supercapacitors) mode at 10 mV s^{-1} in different potential windows. Figure 4.8(c) demonstrates the CV curve with different scan rates ranging from 1 mV s^{-1} to 100 mV s^{-1}. Figure 4.8(d) subsequently, shows GCD studies conducted for measuring the actual capacitance of the electrode using Equation (4.13). The capacitance values were found to be 551 F g^{-1}, 538 F g^{-1}, 520 F g^{-1}, and 396 F g^{-1} at current densities of 0.5 A g^{-1}, 1 A g^{-1}, 2 A g^{-1}, and 3 A g^{-1} respectively. In Figure 4.8(e), the EIS plot (Nyquist) plot was shown in the frequency range 1 MHz to 0.1 Hz at OCP (108 mV) showing higher charge transfer in full ASC (anhydrouCoC2O4//AC) cell. Figure 4.8(f) show the Coulombic efficiency plot of two electrode cell with capacity retention close to 97% of its

initial value after 1700cycles. Specific energy and specific power of asymmetric capacitors were calculated using the following equations:

$$E(\text{W h kg}^{-1}) = \frac{1}{2}\frac{C_{Ascs}}{3.6}V^2 \quad (4.16)$$

$$P(\text{W kg}^{-1}) = \frac{E*3600}{t_{dis}} \quad (4.17)$$

where CASCs is specific capacitance, V is operating voltage and t_{dis} is discharge time.[24] Figure 4.8(g) shows a plot of specific energy (E) vs. specific power (P) at different constant current rates. Resultant values are highest specific energy was found to be 129 W h kg^{-1} at 0.5 A g^{-1} current density with a specific power of ~647 W kg^{-1}. Maximum specific power of ~3890Wkg^{-1} was obtained when specific energy was reduced to ~92 W h kg^{-1} at 3 A g^{-1} of current density

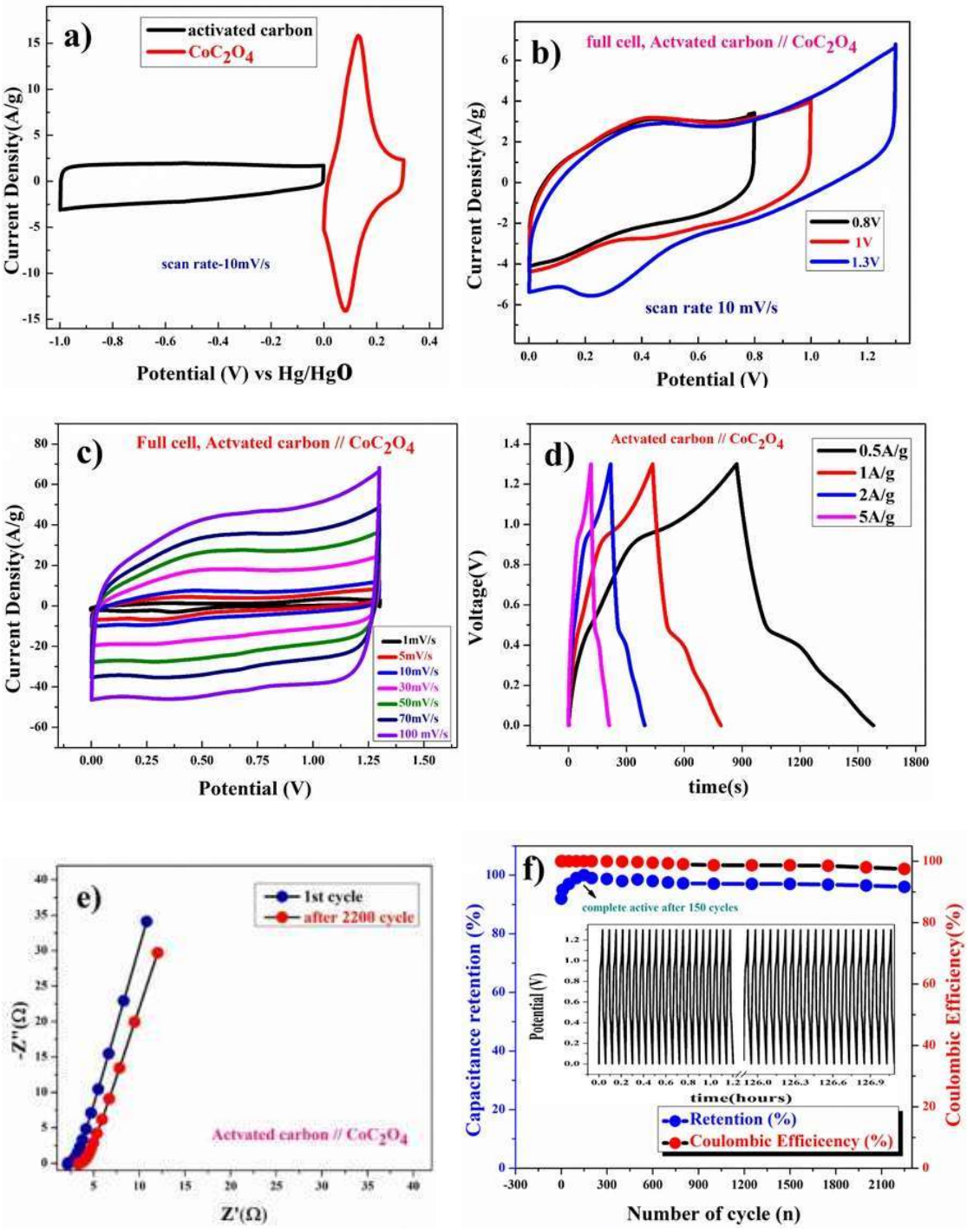
a)
activated carbon
CoC2O4
scan rate-10mV/s
Current Density(A/g)
Potential (V) vs Hg/HgO
b)
full cell, Actvated carbon // CoC2O4
0.8V
1V
1.3V
scan rate 10 mV/s
Current Density(A/g)
Potential (V)
c)
Full cell, Actvated carbon // CoC2O4
1mV/s
5mV/s
10mV/s
30mV/s
50mV/s
70mV/s
100 mV/s
Current Density(A/g)
Potential (V)
d)
Actvated carbon // CoC2O4
0.5A/g
1A/g
2A/g
5A/g
Voltage(V)
time(s)
e)
1st cycle
after 2200 cycle
Actvated carbon // CoC2O4
-Z''(Ω)
Z'(Ω)
f)
complete active after 150 cycles
Potential (V)
time(hours)
Retention (%)
Coulombic Efficiency (%)
Capacitance retention (%)
Coulombic Efficiency(%)
Number of cycle (n)

Continued…

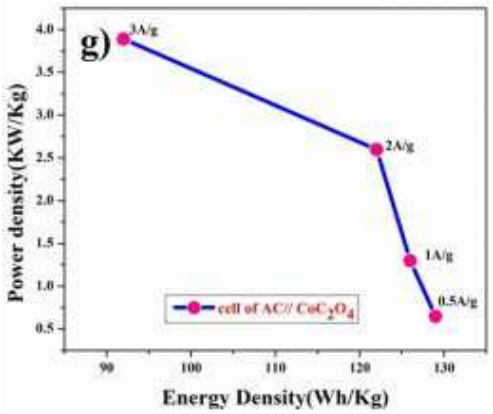

Figure. 4.8: Plot for activated carbon and porous anhydrous CoC_2O_4 cell in ASC mode (a) CV at 10 mV s^{-1}, (b) full cell CV at 10 mV s^{-1} with different voltage window, (c) full cell CV at different scan rate, (d) charge-discharge, (e) EIS at 10 mV, (f) capacitance retention and coulombic efficiency and (g) show plot for activated carbon and porous anhydrous CoC2O4 cell in ASC mode power density and energy density.

A comparison of the capacitance of different Cobalt oxalate-based electrodes is given in Table 4.1.

Material	Morphology	Capacitance (F g^{-1})	Operating potential (V)	Electrolyte	Reference
CoC_2O_4	Thin sheet	1269 at 6 A g^{-1}	0 to 0.5	6 M KOH	33
$Co_{0.5}Mn_{0.4}Ni_{0.1}C_2O_4.nH_2O$	Micro polyhedrons	990 at 0.6 A g^{-1}	0 to 0.4	3 M KOH	13
$CoC_2O_4.2H_2O$	2D porous thin sheets	1.631 F cm^2 at 1.20 mA cm^{-1}	0 to 0.4	6 M KOH	21b
NiC_2O_4	2D thin sheet	2835 F g^{-1} at	0 to 0.4	6 M KOH	34
$Ni_{0.55}Co_{0.45}C_2O_4$	Micro-cuboid	562 C g^{-1} 1A g^{-1}	0 to 0.6	6 M KOH	35
MnC_2O_4/GO	Olive-like	122 F g^{-1} at 0.5 A g^{-1}	-0.1 to 0.55	6 M KOH	36
$CoC_2O_4.2H_2O$	Flakes type	840 F g^{-1} at 1 A g^{-1}	0 to 0.3	2 M KOH	Present work Present work
Anhydrous CoC_2O_4	Nanorods	2116 F g^{-1} at 1 A g^{-1} and1636 F g^{-1} at 1 mV s^{-1}		2 M KOH	Present work
Anhydrous CoC_2O_4	Nanorods	973 F g^{-1} at 1 A g^{-1}	0 to 0.3	0.5 M Na_2SO_4	Present work

Table 4.1:comparison of capacitive performances of different Cobalt oxalate based electrodes

4.8 Conclusions

In summary, porous anhydrous CoC_2O_4 nanorods were successfully synthesized using a two-step process, first $CoC_2O_4.2H_2O$ was synthesized by co-precipitation method in an aqueous medium followed by heating the precipitate at 210 ºC to produce porous CoC_2O_4 nanorods. Porous CoC_2O_4 nanorods showed pseudocapacitive energy/charge storage behavior with a specific capacitance of the materials reaching as high as 2116 F g^{-1} at a current density of $1Ag^{-1}$ with excellent cyclic stability. The predominant intercalative mechanism seems to operate behind high charge storage as intercalative (inner) and surface (outer) charges stored by porous anhydrous CoC_2O_4 were close to as high as 75% and 25% respectively. Porous anhydrous CoC_2O_4// AC full cell resulted in maximum specific energy of 129 W h kg^{-1} and specific power of ~647 Wkg^{-1} at 0.5 A g^{-1} current density in the voltage window of 1.3 V in 2 M KOH electrolyte. These results make porous anhydrous CoC_2O_4 nanorods a potential pseudo-capacitive electrode for large-scale energy storage application in ASC mode.